Direct Imaging of Irregular Satellite Disks in Scattered Light

Loic Nassif-Lachapelle [1], Daniel Tamayo[2]⋆

[1] *Department of Astronomy and Astrophysics, University of Toronto, Toronto, Ontario, M5S 3H4, Canada*

[2] *Department of Astrophysical Sciences, Princeton University, Princeton, New Jersey 08544, United States*

Draft version: 16 August 2021

ABSTRACT

Direct imaging surveys have found that long-period super-Jupiters are rare. By contrast, recent modeling of the widespread gaps in protoplanetary disks revealed by ALMA suggests an abundant population of smaller Neptune to Jupiter-mass planets at large separations. The thermal emission from such lower-mass planets is negligible at optical and near-infrared wavelengths, leaving only their weak signals in reflected light. Planets do not scatter enough light at these large orbital distances, but there is a natural way to enhance their reflecting area. Each of the four giant planets in our solar system hosts swarms of dozens of irregular satellites, gravitationally captured planetesimals that fill their host planets' spheres of gravitational influence. What we see of them today are the leftovers of an intense collisional evolution. At early times, they would have generated bright circumplanetary debris disks. We investigate the properties and detectability of such irregular satellite disks (ISDs) following models for their collisional evolution from Kennedy & Wyatt (2011). We find that ISD brightnesses peak in the $10 - 100$ AU range probed by ALMA, and can render planets detectable over a wide range of parameters with upcoming high-contrast instrumentation. We argue that future instruments with wide fields of view could simultaneously characterize the atmospheres of known close-in planets, and reveal the population of long-period ∼ Neptune-Jupiter mass exoplanets inaccessible to other detection methods. This provides a complementary and compelling science case that would elucidate the early lives of planetary systems.

Key words:

1 INTRODUCTION

Submillimeter observations with the Atacama Large Millimeter Array (ALMA) have revealed that gaps and rings are common features in the brightest, nearby protoplanetary disks (Andrews et al. 2018). Such structures can potentially be explained through a variety of (magneto)hydrodynamic effects (e.g., Takahashi & Inutsuka 2014; Flock et al. 2015; Lorén-Aguilar & Bate 2015; Béthune et al. 2016) or condensation fronts (e.g., Zhang et al. 2015). However, they are most often interpreted as signposts of the formation of giant planets (e.g., ALMA Partnership et al. 2015; Dipierro et al. 2015; Tamayo et al. 2015; Pinte et al. 2015).

By modeling the dust gaps opened by planets of various masses across a range of disk parameters, Zhang et al. (2018) infer that most of the gaps observed by the DSHARP survey (Andrews et al. 2018) are consistent with planets with masses between that of Neptune and Jupiter ($M_N - M_J$). Strikingly, Zhang et al. (2018) infer that the occurrence rate of such planets is ∼ 50%, spread log-uniformly from ∼ $10 - 200$ AU. If correct, this presents at least two important problems for planet formation theory.

First, planet formation theory has difficulties forming giant

planet cores at tens of AU separations from their host star within the ∼ Myr lifetimes of gas disks (see Goldreich et al. 2004, for a review), though pebble accretion may help alleviate the tension (Johansen & Lambrechts 2017; Rosenthal & Murray-Clay 2018). Second, even if giant planet cores can be accreted, they should then undergo fast, runaway accretion to become gas giants once their gas envelope becomes comparable in mass to the solid core (e.g., Pollack et al. 1996; Piso & Youdin 2014; Lee et al. 2014). Why then, would one find ∼ Neptune-mass planets in this short-lived runaway mass-range while gas remains available in the disk for accretion?

Given that a planetary origin for the gap structures found with ALMA would thus provide fundamental constraints on current planet formation theory, observational tests of this hypothesis are a critical effort in exoplanet science and are being vigorously pursued from multiple directions.

One way to do this during the disk phase is to look for perturbations to the disk's gas pressure profile from embedded planets. In this way, Teague et al. (2018) and Pinte et al. (2018) were able to indirectly detect the kinematic signature of Jupiter-mass planets embedded in the HD 163296 disk. Another is to detect planets through their much brighter *circumplanetary* disks in either scattered light (Szulágyi et al. 2019) or thermal emission (Szulágyi et al. 2018). Such searches are currently underway. However, both

⋆ NHFP Sagan Fellow

methods are observationally limited to finding planets $\gtrsim 1 M_J$ more massive than the population suggested by ALMA.

A complementary approach is to search for such a population of distant giant planets following disk dispersal. This has long been the focus of ground-based direct imaging, yielding several of the most iconic exoplanet detections to date, like HR 8799 (Marois et al. 2008) and Beta Pictoris b (Lagrange et al. 2010), and enabling the spectroscopic characterization of these planets' atmospheres (e.g., Janson et al. 2010; Bowler et al. 2010; Chilcote et al. 2014).

However, the conclusion from extensive direct imaging surveys is that planets $\gtrsim 5 M_{Jup}$ are rare beyond a few tens of AU, occurring only around approximately 1% of stars on average (Bowler & Nielsen 2018), though about ten times more frequently around A stars (Nielsen et al. 2019).

At face value this seems to contradict the ∼ 50% planetary occurrence inferred by Zhang et al. (2018). However, their ALMA observations implicate a much lower-mass planet population than is currently accessible through direct imaging. Such a result seems plausible from microlensing (e.g. Gould et al. 2010) and radial velocity (e.g., Cumming et al. 2008) detections in the 1-10 AU range, which suggest that lower-mass ice giants like Neptune are significantly more common than gas giants $\gtrsim 1 M_J$. However, probing this large, putative $M_N - M_J$ population at $> 10 AU$ separations will require pushing direct imaging detections to significantly lower masses.

1.1 Thermal Emission vs. Scattered Light

At face value, the prospects for detecting the abundant population of *long-period* Neptunes implied by the gaps in the DSHARP survey (Zhang et al. 2018) seems bleak for ground-based direct imaging. Detections to date have relied on searching for young planets' thermal emission in the near-infrared. This is in the Wien limit of the blackbody emission, where the emission falls off exponentially as the temperature decreases. Thus, only the hottest, most massive tail of the planet distribution is detectable at early times, dropping sharply toward lower masses and higher ages (Sec. 3).

Next generation direct imaging instruments therefore plan to push toward lower-mass planets by moving to the mid-infrared, or by searching for planets in scattered light. In the latter case, the fraction of starlight intercepted by a planet, and thus its scattered light signal, grows quadratically the closer the planet is to its host star. The optimal giant planet targets at 0.1" separations from nearby stars (corresponding to $\lesssim 5 AU$) yield typical contrast ratios ∼ 10^{-8} (Traub et al. 2014). Larger ELTs will move toward even smaller angular separations with brighter planets, but none of these approaches would constrain the much fainter, population of *long-period, low-mass* Neptunes implied by the gaps in the DSHARP survey (Zhang et al. 2018).

In Fig. 1, we plot the contrast ratios for a population of planets with semimajor axes drawn log-uniformly from 10-200 AU (Zhang et al. 2018), and masses drawn from a power-law $dN/d \log M \propto M^{-0.86}$ between M_N and $13 M_J$, which Clanton & Gaudi (2016) inferred by combining direct imaging, microlensing and radial velocity detections. For the host stars we take an approximation (Sec. 4.2) to the stellar sample of GPIES, the Gemini Planet Imager Exoplanet Survey (Nielsen et al. 2019). The planet fluxes are a combination of scattered light and thermal emission in H band (≈ 1.65μm), using planetary models from Baraffe et al. (2008) with a heavy element mass fraction $Z = 0.02$. This provides optimistic estimates of scattered light from low-mass planets, since in real-
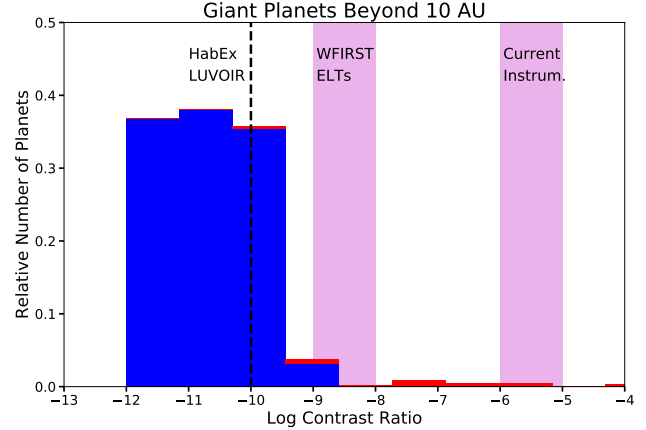

Figure 1. Contrast ratio histogram for the putative population of planets beyond 10 AU inferred from ALMA observations (Zhang et al. 2018), with masses drawn from constraints by Clanton & Gaudi (2016) combining direct imaging, microlensing and radial velocity detections. Planets whose emission is dominated by thermal emission are colored red (all more massive than Jupiter), while planets that dominently scatter incident starlight are in blue. Vertical lines denote fiducial contrast ratio detection thresholds for current and future instrumentation. Most of these planets beyond 10 AU are undetectable for the foreseeable future.

ity they would have higher metal fractions and thus smaller radii and scattering area. Planets whose flux is dominated by this scattered light component are colored in blue, while those that dominantly emit thermally are colored red. All planets dominated by their thermal emission with contrasts > 10^{-8} have masses higher than Jupiter. Low metal fractions are more appropriate for such objects, but higher values of Z would only increase contrast ratios by at most a factor of 2.

On the right of Fig. 1, we highlight in magenta the rough detection threshold for current state-of-the-art instrumentation, where the exact contrast depends on the particular instrument, stellar magnitude and the planet's angular separation from its host (e.g., Ruffio et al. 2017). We also mark contrast goals for next generation direct imaging instruments on WFIRST and 30-m class telescopes (ELTs), as well as the Habitable Exoplanet Explorer (HabEx) and LUVOIR mission concepts, which would launch in the late 2030s.

In summary, while future direct imaging instruments will find and characterize many close-in exoplanets, the prospects for directly imaging the large population of long-period, Neptune-Jupiter mass planets putatively revealed by ALMA seem bleak for the foreseeable future. However, given that planets with masses $\lesssim 1 M_{Jup}$ are brightest in scattered light (in blue, Fig. 1), the best way to improve their detectability is by increasing their scattering surface area, and our own Solar System suggests a natural way to do that.

1.2 Irregular Satellites

In our own solar system, each of the four giant planets hosts large populations of small irregular satellites of a few to ∼ 100 km in diameter, roughly filling their Hill spheres. These are thought to be objects left over from the era of planet formation that were gravitationally captured early in the solar system's history. This results in swarms of mutually inclined, crossing orbits.

This implies an intense collisional evolution, of which we only see the remains. Indeed, by modeling this process, Bottke et al. (2010) infer that irregular satellites represent the most collision-

ally evolved population in the solar system. Debris from such collisions has been detected around Saturn in the mid-infrared (Verbiscer et al. 2009; Hamilton et al. 2015), as well as in scattered optical light (Tamayo et al. 2014, 2016). While the integrated scattered flux from this 'Phoebe Ring' is currently smaller than that of Saturn, at early times it would have been orders of magnitude brighter. Thus, irregular satellite disks (ISDs) could significantly boost exoplanets' scattered light signals, rendering them detectable with current and future instrumentation.

Not only could this help fill in the census of Neptune-Jupiter mass planets at large separations, it would also shed light on the mechanism for irregular satellite capture. Planetesimals encounter isolated planets on hyperbolic trajectories, and thus require a way to lose energy in order to become bound. Pollack et al. (1979) proposed that drag from a circumplanetary gas disk could provide the requisite dissipation. Ćuk & Burns (2004) then showed that this could plausibly explain the prograde group of irregular satellites at Jupiter. However, gas drag continues to operate following capture, leading to eventual loss of these bodies. In this picture, therefore, the surviving irregular satellites are the last generation that was captured near the end of the disk phase.

By contrast, passing planetesimals could also be captured during close encounters between giant planets, losing enough energy from one planet to remain bound to the other. Nesvorný et al. (2007) found that this process could efficiently capture irregular satellites in the dynamical instability scenario envisioned by Tsiganis et al. (2005) for the early solar system.

While the dominant capture mechanism remains uncertain, both the above processes are generic in planetary systems. Large planets must accrete in gaseous environments, and the distribution of giant exoplanets' orbital eccentricities is well reproduced by planetary close encounters (Chatterjee et al. 2008; Jurić & Tremaine 2008).

Detecting a sample of ISDs would not only help differentiate between these scenarios, it would also elucidate the early stages of planetary system assembly. Most directly, discovery of gaseous giant planets at long orbital periods challenges theories to form them before disk dispersal. This may point to processes such as pebble accretion that can speed up growth (Lambrechts & Johansen 2012; Rosenthal & Murray-Clay 2018). Additionally, the rain of ISD debris onto the central accreting protoplanet atmosphere could provide a significant opacity source, which would act to delay cooling and stall accretion (Piso & Youdin 2014; Lee & Chiang 2015; Brouwers & Ormel 2019). This could help explain how large numbers of Neptunes managed to accrete some gas without running away to form Jovian planets. Alternatively, if irregular satellites are captured during planetary encounters, ISDs would provide signposts for the timing of instabilities in young planetary systems.

This motivates investigating the collisional evolution of ISDs, both in order to inform their expected brightnesses, and the optimal observational strategies to find them. Kennedy & Wyatt (2011) (henceforth K11) developed such models, applying them both to our own solar system's ISDs and the directly imaged object Fomalhaut b (Kalas et al. 2008, 2013). They also considered prospects for space-based follow-up with the Hubble and James Webb Space Telescopes. Here we instead focus on their implications for observations with ground-based instruments, as well as WFIRST and the HabEx and LUVOIR mission concepts.

In Sec. 2 we recapitulate the model of K11. We then combine these results into analytic estimates of expected ISD contrast ratios in Sec. 3, discuss their implications for observational strategies, and describe their observational signatures. In Sec. 4 make projections

for current and future instrumentation using a target sample optimized for such ISD detections. We summarize and conclude in Sec. 5.

2 MODEL

2.1 Contrast Ratios

The contrast ratio at wavelength λ of starlight scattered off an astrophysical object is simply the fraction of light intercepted by the object's geometrical cross-section σ, multiplied by its single-scattering albedo Q and phase function g (e.g., Collier Cameron et al. 2002),

$$C(\lambda) = g(\alpha, \lambda)Q(\lambda)\frac{\sigma}{\pi a^2}, \tag{1}$$

where a is the planet's semimajor axis, and g is additionally a function of the phase angle of observation α. Following Collier Cameron et al. (2002) and K11, we set g to a nominal value of 0.32, the value for a Lambert sphere at maximum elongation from its host star. Specializing to ISDs, we take the single-scattering Bond albedo of ≈ 0.1 measured for dust grains in Saturn's ISD, the Phoebe ring (Tamayo et al. 2014, 2016),

$$C \approx 1.0 \times 10^{-12} \left(\frac{g}{0.32}\right)\left(\frac{Q}{0.1}\right)\left(\frac{90\text{AU}}{a}\right)^2\left(\frac{\sigma}{\pi R_J^2}\right). \tag{2}$$

The normalization of σ to Jupiter's cross-sectional (πR_J^2) area shows that detecting a Jupiter directly in scattered light at tens of AU from its host star is far beyond the reach of current or planned technology. However, an ISD can boost the scattering surface area σ by orders of magnitude.

2.2 Area-To-Mass Ratio

We assume a steady state collisional cascade with the number of satellites $n(D)dD$ with diameter between D and $D + dD$ given by $n(D) \propto D^{2-3q}$. Following K11, we consider a broken power law separating small bodies, which are dominantly held together by their material strength, from large bodies held together by self-gravity. In particular, we take a power-law index $q = q_s$ from size D_{min} to D_t, and $q = q_g$ from size D_t to the maximum satellite size that participates in the cascade D_c.

For typical particle size distributions, most of the surface area is in the smallest grains, while most of the mass is in the largest bodies. We will assume this throughout the paper. The disk brightness, set by the rate at which the collisional cascade is fed, is therefore determined by the mass liberated through collisions of the largest moons of size D_c (Wyatt et al. 2007). It is therefore instructive to express the surface area in terms of the disk mass M through the cascade's area-to-mass ratio ξ, so $\sigma(t) = \xi M(t)$.

Because the initial mass and surface area are both simply proportional to the normalization of $n(D)$ above, they depend linearly on one another. Thus, the disk's area-to-mass ratio ξ is independent of both time and the total amount of material, and is set only by the parameters of the cascade. To give concrete scalings, we take K11's nominal parameters of $q_s = 1.9$, $q_g = 1.7$, in which case,

$$\left(\frac{\xi}{\pi R_J^2/M_\oplus}\right) \approx 5.5 \times 10^6 \left(\frac{\rho}{\text{g/cc}}\right)^{-1}\left(\frac{D_c}{100\text{ km}}\right)^{-0.9}\left(\frac{D_t}{100\text{ m}}\right)^{0.6}\left(\frac{D_{min}}{\mu\text{m}}\right)^{-0.7}, \tag{3}$$

where $M_\oplus$ is the mass of the Earth. For a fixed initial mass budget

M_0 at time $t = 0$, one can thus increase σ (through ξ) by either decreasing D_c, liberating mass in the small area-filling particles, or by decreasing $D_{\min}$ and similarly increasing the number of small grains.

For the nominal parameters above, this implies that a $1M_\oplus$ collisional cascade would boost a planet's contrast ratio by almost 7 orders of magnitude; we comment further on reasonable mass scales in Sec. 4. Finally, while the nominal parameter values in Eq. 3 are reasonable for all the solar system's irregular satellite populations, the minimum particle size D_{min} will vary substantially with stellar mass.

The minimum particle size is set by radiation pressure moving small grains onto near-radial circumplanetary orbits, and depends on their orbital distance around the planet (Burns et al. 1979). Following K11, we take a characteristic separation from the planet η, expressed as a fraction of the planet's Hill sphere. In that case, the minimum grain diameter is independent of the planet's semimajor axis, and given by (K11)

$$\frac{D_{min}}{\mu\text{m}} \approx 2 \left(\frac{\eta}{0.3}\right)^{1/2} \left(\frac{M_\star}{0.5M_\odot}\right)^{10/3} \left(\frac{M_p}{M_J}\right)^{-1/3} \left(\frac{\rho}{\text{g/cc}}\right)^{-1}, \quad (4)$$

where we have used that $L_\star/L_\odot \sim (M_\star/M_\odot)^4$ (Popper 1980) to emphasize the strong dependence of radiation pressure on stellar mass.

Equations 3 and 4 suggest that one can continue increasing the surface area of circumplanetary swarms by moving toward lower-mass stars and thus decreasing D_{min}. However, one eventually reaches a floor where D_{min} becomes comparable to the wavelength of observation (e.g., $\approx 1.65\mu\text{m}$ when observing in H band with GPI). At this point, observing even lower-mass stars no longer helps, since even though smaller, higher surface-area grains might exist, they can no longer effectively scatter photons at the wavelength of observation. When observing in the near-infared, using the nominal parameters in Eq. 4, this transition occurs at $M_\star \approx 0.5M_\odot$, or roughly M1 stars. We therefore normalize Eq. 4 at this optimum target mass, noting that our subsequent equations are only valid for $M_\star > 0.5M_\odot$. This is also roughly applicable even at shorter observation wavelengths, since although the observation wavelength would suggest targeting lower-mass stars, one would instead become limited by the star's spectrum peaking at longer wavelengths.

2.3 Collisional Timescales

Following Wyatt et al. (2010), K11 estimate a collision rate for the largest bodies of size D_c that participate in and feed the cascade (Sec. 2.4) through a particle-in-a-box formalism. In this approximation, the rate of collisions for a moon of diameter D_c is the product of the number density of impactors and the rate at which it sweeps out volume $\pi D_c^2 v_{\text{rel}}$, where v_{rel} is a characteristic relative velocity. Throughout this paper set this relative speed to the circular Keplerian velocity at a semimajor axis ηR_H around the planet, times a factor of $4/\pi$ as appropriate for a swarm of circular, isotropic orbits. Using more sophisticated methods, K11 estimate that this analytical result is correct within $\approx 30\%$ for typical parameters. Finally, K11 consider that the energy per target mass needed to shatter and disperse a body of size D_c with gravity-dominated strength, is

$$\frac{Q_D^*}{\text{J/kg}} = \frac{3.3 \times 10^4}{f_Q} \left(\frac{\rho}{\text{g/cc}}\right)\left(\frac{D_c}{100 \text{ km}}\right)^{1.26}, \quad (5)$$

where f_Q is a factor parametrizing the uncertainty in this quantity, which can vary by about an order of magnitude for various col-

lision geometries and between different studies (e.g. Benz & Asphaug 1999; Leinhardt & Stewart 2009). Bottke et al. (2010) find $f_Q > 3$ best fit the solar system irregular satellites, and K11 adopted $f_Q = 5$. Considering only collisions with bodies in the cascade with sufficient kinetic energy to disrupt a moon of size D_c yields a collisional timescale for the largest bodies T_{col} inversely proportional to the number of potential impactors and thus to the total mass M of the ISD (K11),

$$\frac{T_{col}}{10 \text{ Myr}} = f_a^{-4.13} \left(\frac{M_p}{M_J}\right)^{0.24} \left(\frac{M_\star}{0.5 \ M_\odot}\right)^{-1.38} \left(\frac{a}{90 \text{ AU}}\right)^{4.13} \left(\frac{M}{M_\oplus}\right)^{-1}, \quad (6)$$

where the swarm-specific parameters have been collected in the dimensionless parameter f_a defined as

$$f_a \approx \left(\frac{f_Q}{5}\right)^{0.15} \left(\frac{\eta}{0.3}\right)^{-1} \left(\frac{\rho}{\text{g/cc}}\right)^{-0.39} \left(\frac{D_c}{100 \text{ km}}\right)^{-0.43}. \quad (7)$$

The reference values have been chosen from the solar system irregular satellites, so f_a should be of order unity, and its exponent in Eq. 6 was chosen to simplify the interpretation of later expressions.

We briefly note several trends (for a deeper discussion see K11). The strongest dependence is on a, largely since the Hill sphere's volume that must be explored for collisions to occur is proportional to a^3. More subtly, if bodies orbit within a fixed fraction η of the Hill sphere, the relative velocities get slower with increasing semimajor axis of the planet, reducing the ability to break up large bodies. Collision times also get longer the smaller the available mass of impactors in the ISD M, so collision timescales will grow as the ISD grinds down with time. There is also a near-inverse dependence on the stellar mass, largely because the Hill sphere's volume that must be explored for a collision is inversely proportional to $M_\star$.

For the swarm parameters encoded in f_a, the strongest dependence is on the size of the largest bodies in the collisional cascade D_c. The larger D_c is, the fewer such bodies there can be for a fixed swarm mass, so it's harder for potential destructors to find these bodies as they wander the planet's Hill sphere. It is also harder to break up larger bodies because self-gravity better holds them together.

Finally, as K11 note, there is a very weak dependence on planet mass, with important implications that we discuss in Sec. 3.1. While increasing the planet mass linearly increases the Hill sphere's volume in which collisions occur, it also speeds up the rate at which this phase space is explored by shortening the orbital periods. Additionally, the larger relative velocities make it possible for comparatively smaller impactors to disrupt the largest bodies in the cascade.

2.4 Mass time evolution

Following K11, we assume that the size distribution remains fixed and that mass is lost from the cascade by the breakup of the largest objects of size D_c, in which case (Wyatt et al. 2007),

$$\dot{M} = -\frac{M}{T_{\text{col}}} \propto -M^2, \quad (8)$$

since $T_{\text{col}} \propto M^{-1}$. One can verify through direct substitution that the solution is given by (Wyatt et al. 2007),

$$M(t) = \frac{M_0}{1 + t/T_{\text{col}}(M_0)}, \quad (9)$$

where M_0 is the initial mass of the ISD. Thus, for $t \ll T_{\text{col}}(M_0)$, the mass remains fixed at the initial value because not enough time

has elapsed for collisions. We will refer to such a regime as an age-limited disk, since the breakup of the largest bodies that feed the cascade is limited by the age of the system.

For $t \gg T_{\mathrm{col}}(M_0)$, one can ignore the sum in the denominator, and the factor of M_0^{-1} in T_{col} (Eq. 6) cancels with the numerator to yield $M_{\mathrm{tot}}(t) \propto t^{-1}$, *independent of the initial mass* (Wyatt et al. 2007). Physically, this is because the mass-dependence of the collision timescale (Eq. 6) regulates the rate of grind-down. More massive disks collide and grind down faster, while less massive disks 'wait' for their more massive counterparts to catch up, leading different initial masses to converge to the same late-time evolution (Fig. 2). Following Heng & Tremaine (2010), we will refer to this regime as a collision-limited disk.

Given that the strongest dependence is on the semimajor axis (Eq. 6), K11 calculate the optimum value of a at which to find an ISD, fixing all other parameters. This corresponds to finding the transition between the age-limited and collision-limited regimes, where the largest bodies have only just started colliding and haven't substantially ground down, i.e. where the collision time T_{col} is equal to the age of the system T_{age}. Inverting Eq. 6 then yields an optimum semimajor axis a_{opt},

$$\frac{a_{opt}}{90\,AU} = f_a \left(\frac{M_p}{M_J}\right)^{-0.06} \left(\frac{M_\star}{0.5\,M_\odot}\right)^{0.33} \left(\frac{M_0}{M_\oplus}\right)^{0.24} \left(\frac{T_{age}}{10\,\mathrm{Myr}}\right)^{0.24}. \quad (10)$$

Thus, f_a can be interpreted as the order-unity factor by which the swarm-specific parameters (Eq. 7) change the optimimum semimajor axis at which the ISD contrast ratio peaks.

An intuitive approximation of the mass evolution is that for $a > a_{opt}$, the largest bodies have not yet had time to disrupt, so $M \approx M_0$, while for $a < a_{opt}$ the debris disk has converged to a state in which the collision time of the largest bodies is equal to the system's age[1] (Heng & Tremaine 2010), and the remaining mass is independent of M_0 (Fig. 2). Combining Eqs. 6 and 9,

$$\left(\frac{M}{M_\oplus}\right) \approx \begin{cases} f_a^{-4.13} \left(\frac{M_p}{M_J}\right)^{0.24} \left(\frac{M_\star}{0.5\,M_\odot}\right)^{-1.38} \left(\frac{a}{90\,AU}\right)^{4.13} \left(\frac{10\,\mathrm{Myr}}{T_{age}}\right) & a < a_{opt} \\ M_0/M_\oplus & a > a_{opt} \end{cases} \quad (11)$$

As a nominal example, we take an ISD around a Jupiter-mass planet around TWA 13A, an $\approx$ 8th magnitude M1 star in H band, at $\approx$ 55 pc in the TWA association (Gagné et al. 2017), which is estimated to be $\approx$ 7.5 Myr old (Ducourant et al. 2014; Donaldson et al. 2016). We assume a fiducial stellar mass of $0.5M_\odot$, a luminosity of $0.06L_\odot$, and the nominal ISD parameters given in Eq. 7. We plot in Fig. 2 the remaining ISD mass around planets of different semimajor axes for 4 different initial ISD masses (blue curves) of $1, 10^{-2}, 10^{-4}$ and $10^{-6} M_\oplus$.

The dashed red line is the approximation for $a < a_{opt}$ in the collision-limited regime (Eq. 11), to which all initial masses converge. The mass estimate in this collision-limited regime is therefore particularly simple. For example, at a semimajor axis of 10 AU, all initial masses converge to the same value of $\approx 10^{-4} M_\oplus$ in Fig. 2, unless the initial mass was smaller than this value. This would mean that there hasn't been enough time for the largest bodies in this swarm to collide, and the ISD mass remains at its initial value (e.g., the bottom curve, which remains at its initial value of $10^{-6} M_\oplus$).

---

[1] This can be seen quantitatively by setting $T_{\mathrm{col}} = t$ in Eq. 8, which yields the same late-time solution $M \propto t^{-1}$.

3 CONTRAST RATIO SCALINGS AND OBSERVATIONAL SIGNATURES

The strongest dependence is on the planet's semimajor axis, since that strongly influences the number of collision timescales the ISD has experienced and how much it has ground down. So despite the fact that the fraction of intercepted starlight falls off quadratically with distance (Eq. 1), the remaining mass in the collision-limited regime increases with semimajor axis even more steeply (Eq. 11). Thus, the contrast ratio will grow with semimajor axis until it reaches a_{opt}, beyond which the mass remains at its initial value (Fig. 2), and the contrast then simply falls off quadratically with distance.

We can therefore calculate the maximum contrast ratio by combining Eqs 1 and 3, assuming $M = M_0$ at $a = a_{opt}$. This yields

$$C_{max} = 3.3{\times}10^{-6} f_{Cmax} \left(\frac{M_p}{M_J}\right)^{0.34} \left(\frac{M_\star}{0.5\,M_\odot}\right)^{-3.0} \left(\frac{T_{age}}{10\mathrm{Myr}}\right)^{-0.48} \left(\frac{M_0}{M_\oplus}\right)^{0.52}, \quad (12)$$

with swarm-specific parameters collected in f_{Cmax},

$$f_{Cmax} = \left(\frac{g}{0.32}\right) \left(\frac{Q}{0.1}\right) \left(\frac{f_Q}{5}\right)^{-0.31} \left(\frac{\rho}{\mathrm{g/cc}}\right)^{0.5} \left(\frac{D_t}{100\mathrm{m}}\right)^{0.6} \left(\frac{D_c}{100\mathrm{km}}\right)^{-0.03} \left(\frac{\eta}{0.3}\right)^{1.65}. \quad (13)$$

This allows us to write an approximate solution for the contrast ratio in compact form,

$$C \approx \begin{cases} C_{max} \left(\frac{a}{a_{opt}}\right)^{2.13} & a < a_{opt} \\ C_{max} \left(\frac{a}{a_{opt}}\right)^{-2} & a > a_{opt} \end{cases} \quad (14)$$

We plot exact solutions to the collisional model of K11 in blue lines in Fig. 3 for the same initial masses as Fig. 2, together with the top branch of Eq. 14 as a dashed red line. The exact solutions peak at $C_{max}/2$, since at $a = a_{opt}$, $t = T_{col}$ by definition, so M_0 has dropped by a factor of two through Eq. 9.

We note that C_{max} depends on the initial mass in irregular satellites M_0 (the peaks in Fig. 3 scale as $\approx M_0^{0.5}$ through Eq. 12), because that sets how far out the collision-limited regime extends in Fig. 3 before reaching a_{opt} through Eq. 10. But in the collision-limited regime, this dependence cancels out as it should. Plugging Eq. 12 and 10 into Eq. 14 yields for the collision-limited regime ($a < a_{opt}$)

$$C = 3.3 \times 10^{-6} f_C \left(\frac{M_p}{M_J}\right)^{0.47} \left(\frac{M_\star}{0.5\,M_\odot}\right)^{-3.71} \left(\frac{a}{90\mathrm{AU}}\right)^{2.13} \left(\frac{10\,\mathrm{Myr}}{T_{age}}\right), \quad (15)$$

with f_C,

$$f_C = \left(\frac{g}{0.32}\right) \left(\frac{Q}{0.1}\right) \left(\frac{f_Q}{5}\right)^{-0.63} \left(\frac{\rho}{\mathrm{g/cc}}\right)^{1.33} \left(\frac{D_t}{100\mathrm{m}}\right)^{0.6} \left(\frac{D_c}{100\mathrm{km}}\right)^{0.89} \left(\frac{\eta}{0.3}\right)^{3.78}. \quad (16)$$

Putting everything together, it is interesting to note that the parameter f_{Cmax} (Eq. 13) is fairly insensitive to its constituent swarm parameters. This is because the two other combinations f_a (Eq. 7) and f_C (Eq. 16) are anti-correlated. Swarm parameters that raise f_C and move all the curves in Fig. 3 upward tend to reduce f_a, so the
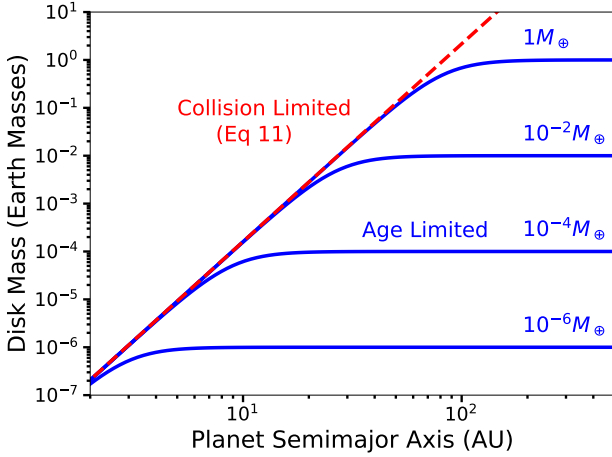
Figure 2. Remaining disk mass as a function of semimajor axis for four different initial ISD masses (blue curves, with stellar and ISD parameters given in text). At wide separations in the age-limited regime, the largest bodies in the ISD have not yet had time to collide, and the masses remain at their initial values. At closer separations, i.e., after many collision timescales, all curves converge onto the collision-limited approximation (dashed red line), so the mass becomes independent of the initial mass and given by the second case in Eq. 11. The transition from the age-limited to collision-limited regime happens at different locations a_{opt} for different initial masses, given through Eq. 10.
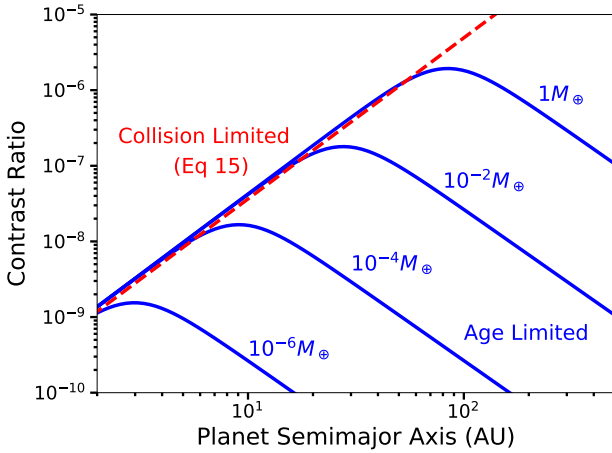

Figure 3. Contrast ratios as a function of semimajor axis for the same ISDs as in Fig. 2. At large separations, in the age-limited regime, the mass remains constant (Fig. 2), so contrasts fall off quadratically as the fraction of intercepted starlight. At smaller separations, all tracks converge onto the same late-time evolution given by Eq. 15 (red dashed line).

blue curves peak at smaller semimajor axes, which has the opposite effect of lowering contrasts. This renders contrast projections reasonably consistent despite the large number of uncertain parameters. We quantify these expected variations over reasonable ranges of parameters in Sec. 4.

3.1 Comparison with Planetary Thermal Emission

The strongest differences searching for ISDs vs planets in thermal emission is the much weaker dependence on planetary mass and time (Eq. 15). As mentioned in Sec. 2.3, the weak ISD contrast ratio dependence on planetary mass is due to competing effects: more

massive planets have larger Hill spheres to explore for collisions (and can host smaller, higher surface-area grains), but also have higher circumplanetary velocities that speed up the rate at which phase space is explored and collisions occur. This weak scaling is in stark contrast to current detections of super-Jovian planets in thermal emission, which fall off precipitously toward lower masses.

Second, contrast ratios decay as t^{-1} (Eq. 15), such that the collisional timescale between the largest bodies in the cascade remains fixed to the age of the system (Sec. 2.3). This scaling is also much shallower than for detections in planetary thermal emission, given that the contrast ratios are extremely strong functions of the cooling planets' temperatures.

We compare these scalings for illustration in Fig. 4, interpolating models for the planetary emission from Baraffe et al. (2008). For simplicity we assume a constant heavy element enrichment fraction $Z = 0.02$. We take a 10 Myr old, $0.5M_\odot$ M1 host with a planet at 60 AU. The left panel varies the planet mass, reflecting the weak ISD dependence on this parameter in Eq. 12, and the much steeper fall-off in planetary thermal emission. In the right panel we plot the contrast ratio as a function of time for a 2 Jupiter-mass planet, showing the significantly shallower time decay for ISDs.

3.2 ISDs are Typically Unresolved

The angular size of an ISD θ_{ISD} is given by the ratio of the planet's Hill sphere radius to the target's distance from Earth,

$$\theta_{ISD} \approx \frac{R_H}{d} = \theta_p \left(\frac{M_p}{3M_\star} \right)^{1/3}, \qquad (17)$$

where θ_p is the angular separation of the planet from the star. Thus, given that detections are typically made near the inner working angle at a θ_p of only a few resolution elements, the mass ratio factor < 0.2 implies that ISDs will typically be unresolved. However, with large fields of view like the 10" of the IRDIS instrument on SPHERE, large-separation detections of giant planets could yield resolved ISDs. While this may complicated the image processing, it provides a straightforward way to identify large-separation ISDs.

3.3 ISDs are Optically Thin

Taking the total surface area of debris $\sigma = M\xi$ as a fraction of the total ISD cross-sectional area πR_H^2 yields an optical depth τ. Assuming the nominal swarm parameters in Eq. 3 then yields,

$$\tau \approx 0.025 \left(\frac{a}{100\text{AU}} \right)^{-2} \left(\frac{M_p}{M_J} \right)^{-2/3} \left(\frac{M_\star}{M_\odot} \right)^{2/3} \left(\frac{M}{M_\oplus} \right). \qquad (18)$$

Therefore, since M is expected to be $\lesssim 1M_\oplus$ (Eq. 11 and Sec. 4.1), ISDs should typically be optically thin, even at early times.

3.4 ISD Scattered Light Should be Polarized

In this optically thin limit, where single scattering dominates, one expects a strong polarization signature (e.g., Kruegel 2003). Given that background stars or galaxies would not yield strong polarization, this would allow instruments with polarimetry modes, like those on GPI and SPHERE, to rule out false positives with a single epoch of observation. Additionally, it would make it possible to more aggressively suppress unpolarized speckle noise, and enhance sensitivity.
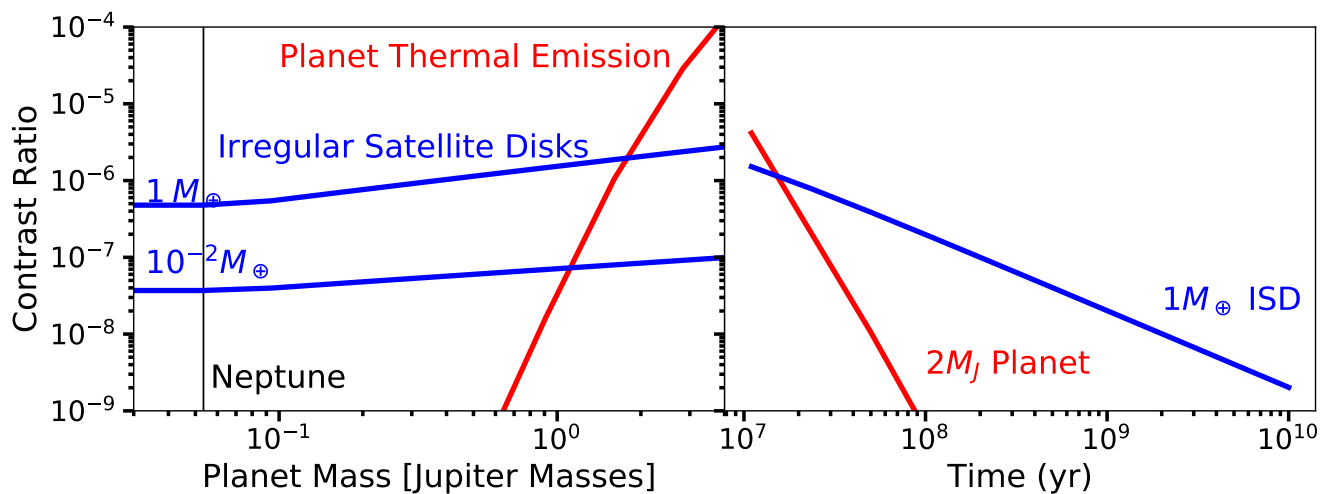
Figure 4. Left panel plots contrast ratio vs planet mass for the same ISD and system parameters as Figs. 2 and 3. Planet is placed at 60 AU separation. Planet thermal emission is interpolated from Baraffe et al. (2008) (see text). ISD scattered light has only a weak dependence on its central planet's mass, allowing for the detection of Neptune-like planets for which thermal emission is undetectable. Right panel plots the same ISD's contrast ratio decay as a function of time for a 2 Jupiter-mass planet. ISD contrast ratios decay slower over time, allowing for a larger window of detectability.

4 PROJECTIONS

With an analytic understanding of the most important scalings, we now make projections sampling parameters from reasonable ranges and optimizing the observation strategy.

4.1 Masses

While the scalings on most swarm parameters are weak (Eq. 13) and expected values reasonably bracketed by those for our own populations of irregular satellites, the largest uncertainty is in the initial mass of the ISD M_0. Here again we can look to our own solar system. The steep size distributions of irregular satellites $\lesssim 10$ km across, and much shallower slopes at larger sizes suggests that the largest irregulars were once part of the collisional cascade and later became stranded as the ISD ground down (Bottke et al. 2010; Kennedy & Wyatt 2011). The largest moons dominate their respective ISD masses, and range from $\approx 0.5 - 5 \times 10^{-6} M_\oplus$ around each of the giant planets.

To estimate the factor by which they have ground down, we assume that the irregular satellites were captured during the gas disk phase at 3 Myr, either through gas drag (Pollack et al. 1979; Ćuk & Burns 2004; Ćuk & Gladman 2006) or three-body encounters (Nesvorný et al. 2007)[2]. If we then take the times estimated by K11 until the largest irregulars become stranded (t_{nleft} in their Table 1), this yields the number of collision times each swarm has experienced, and through Eq. 9 the initial mass M_0. This exercise yields initial ISD masses in the range of $M_0 \sim 10^{-4} M_\oplus$ (Jupiter) - $10^{-2} M_\oplus$ (Neptune). These numbers are of course significantly uncertain, and one might also expect large variations across planetary systems (with extrasolar systems estimated to typically have $\sim 1-5$

times more solid material Chiang & Laughlin 2013). Nevertheless they provide a nominal reference scale, which we take as $10^{-3} M_\oplus$, and explore a wide range around it.

4.2 GPIES Limits

We begin by asking whether such structures would already have been detected by direct imaging surveys if they were prevalent in young planetary systems. As above, we draw planets with semimajor axes drawn log-uniformly from 10-200 AU (Zhang et al. 2018), and masses drawn from a power-law $dN/d \log M \propto M^{-0.86}$ between M_N and $13 M_J$ Clanton & Gaudi (2016). For the host stars we take the public stellar sample of GPIES, the Gemini Planet Imager Exoplanet Survey (Nielsen et al. 2019), and for stellar parameters not available through VizieR catalogues (Ochsenbein et al. 2000), we adopt rough stellar parameters by interpolating their masses, luminosities and temperatures from values in (Popper 1980). We adopt an optimistic log-uniform age distribution for the sample, from 10-100 Myr, which would tend to inflate contrast ratios.

For the swarm parameters, we first fix the phase function $g = 0.32$, the value for a Lambert sphere at maximum elongation. We then adopt the ranges in Table 1, centered on typical values for the irregular satellites in our solar system. The albedo of dust grains in the Phoebe ring is ≈ 0.1 (Tamayo et al. 2011) For our ISD simulation we sample from the range [0.05, 0.25], spanning roughly a factor of 2 in either direction. Irregular satellites in the solar system vary from a few to ~ 100 km in size. We therefore choose to sample the maximum moon size D_C log-uniformly from a wide range of $[10^4, 10^6]$ km. We sample densities log-uniformly from the density of ice to that of silicates, and the transition size between the gravity and strength-dominated regimes by a factor of ten around the nominal value of 100 m adopted by K11. Irregular satellites' characteristic orbital radius η is well constrained between $\approx 0.2 - 0.4$ of their planet's Hill radius. Finally, we sample the uncertain collisional breakup scaling factor log-uniformly from [1,10].

For the main uncertainty in M_0, we take an optimistic initial mass in irregular satellites of $1 M_\oplus$. Given that the solar system is thought to require several tens of Earth masses of planetesimals to

---

[2] In Nesvorný et al. (2007) they actually consider a later capture after several hundred Myr, picturing a Nice model instability scenario timed to explain the so-called Late Heavy Bombardment (LHB). However, cratering during the LHB is now thought to have been more gradual (Morbidelli et al. 2018), and early instabilities may be favored (see, e.g., Deienno et al. 2017; Nesvorný 2018).

Parameter	Range	Description
D_t	10-1000 m	Transition between strength & gravity regimes.
D_c	10-1000 km	Largest body in the collisional cascade.
g	0.32	Phase function
Q	0.05-0.25	Geometric albedo
ρ	1-3 g/cm^3	Bulk density
η	0.2-0.4	Irregulars' orbital radius, relative to R_H
f_Q	1-10	Q_D scaling factor (Eq. 5)
M_0	$1 M_\oplus$	Initial swarm mass.

Table 1. List of swarm parameters, descriptions, and adopted ranges from Monte Carlo simulation
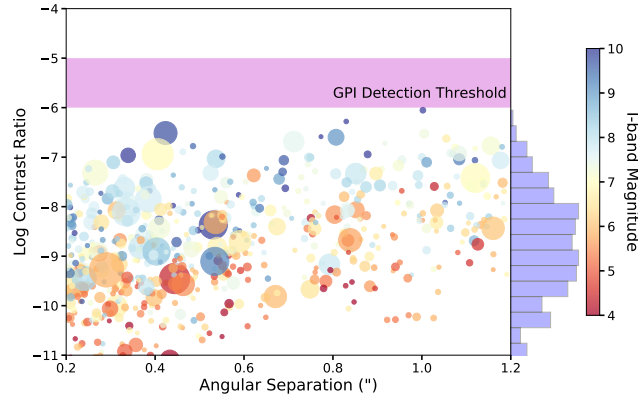
Figure 5. Contrast ratios of ISD realizations for planets around stars in the GPIES survey sample. Even assuming optimistic ISD swarm parameters, one would not expect the GPIES survey to have detected any such structures.

survive accretion in order to drive giant planet migration (Tsiganis et al. 2005), the available mass of potential irregular satellites in an annulus of half-width a planet's Hill radius (e.g. Schlichting 2014) is

$$M_{\text{total}} \sim 1.3 \left(\frac{M_p}{M_{\text{Nep}}} \right)^{1/3} \left(\frac{a}{10 \text{AU}} \right)^{1/2} M_\oplus, \tag{19}$$

where we have assumed that the surface density scales as $a^{-3/2}$ like the minimum-mass solar nebula. Much of this mass would be scattered away, but it sets a natural optimistic mass scale.

We plot the result in Fig. 5. The histogram on the right tallies detections, and the color corresponds to the star's I-band magnitude, which is the relevant wavelength band for the instrument's adaptive optics system. It shows that GPIES not detecting ISDs was expected, even assuming optimistic ISD parameters.

There is a trend of increasing contrast ratio toward fainter stars, which can be simply understood. Given a fixed field of view of $\approx 0.2 - 1.2$", larger distances to the target star d correspond linearly to larger semimajor axes. Thus, the contrast ratio in the collision-limited regime scales as $M_\star^{-3.71} d^{2.13}$ (Eq. 15), or approximately inversely with the star's bolometric flux $\sim M_\star^4 d^{-2}$.

4.3 Maximizing Contrast Ratios

We now consider how target samples could be optimized for the detection of ISDs. Equation 15 suggests a strong preference toward

lower-mass stars, with contrast ratios peaking around $\approx$ M0-M1 hosts[3].

As in the case of imaging planets in thermal emission, it is valuable to search for ISDs around young stars, before the swarms have ground down substantially. This would motivate a similar observation strategy to current direct imaging surveys of searching stars in young moving groups. However, for ISDs, one would additionally aim for the field of view to match reasonable values of a_{opt}, where the contrast ratio peaks. The small exponent in Eq. 10 constrains this range to $\sim 10 - 100$ AU despite large uncertainties in the initial ISD mass.

This highlights the value of a wide field of view like that of the IRDIS instrument on SPHERE (5.5"). Such an instrument can observe the closest young moving groups like the ≈ 25 Myr old β Pictoris moving group at $\approx 20 - 50$ pc from the Sun(Zuckerman et al. 2001; Malo et al. 2014), and still span the whole range of likely a_{opt} from ~ 10-100 AU. Instruments with smaller fields of view ≈ 1" would be more sensitive on stars in slightly more distant young moving groups like the ≈ 8 Myr old TW Hydra association (TWA) at $\approx 40 - 60$ pc from the Sun (De La Reza et al. 2006; Ducourant et al. 2014).

4.4 The Photon-Noise limit

While current ground-based imaging is most often dominated by speckle noise, as the next generation instruments like WFIRST push toward lower contrasts, they will increasingly become photon-noise limited.

In this limit, the relevant metric of detectability is the number of photons arriving at the observer from the planet $\propto C \times L_\star$. Taking again $L_\star/L_\odot \sim (M_\star/M_\odot)^4$ (e.g. Popper 1980) would therefore leave detectability only very weakly dependent on stellar mass in the collision-limited regime (Eq. 15). Thus, in the photon-noise limited regime, there is no particular preference toward low-mass stellar targets; however, ISD contrast ratios around high-mass stars would have proportionately lower contrast ratios following Eq. 15.

Finally, for narrow fields of view in the photon-noise limited regime (as might be applicable for WFIRST), there is no strong dependence on the distance from the observer to the target star d. Here the detectability is $\propto C \times L_\star/d^2$. Putting the same star twice as close to the observer would increase the flux by a factor of four, but since the semimajor axes probed in the fixed field of view are now twice as small, the contrast ratios have also dropped by approximately a factor of four through Eq. 15, rendering the number of photons scattered from an ISD into the detector approximately constant. This relative insensitivity to target distance or mass implies that follow-up observations with WFIRST-CGI of young directly imaged planets would have the added benefit of plausibly making serendipitous discoveries of lower-contrast ISDs in the same systems.

4.5 Projections

Finally, we ask what contrast ratios one would expect with a target sample optimized for finding ISDs. For simplicity, we consider nominal M1 target stars (with mass $M_\star = 0.5 M_\odot$, luminosity $L_\star = 0.035 L_\odot$, and temperature of 3600K) in the β Pictoris moving

---

[3] At masses $\lesssim 0.5 M_\odot$, the minimum particle size in the ISD becomes smaller than observation wavelengths in the optical and near-infrared, as well as the peak of the stellar emission, limiting contrast gains (Sec. 2.2).
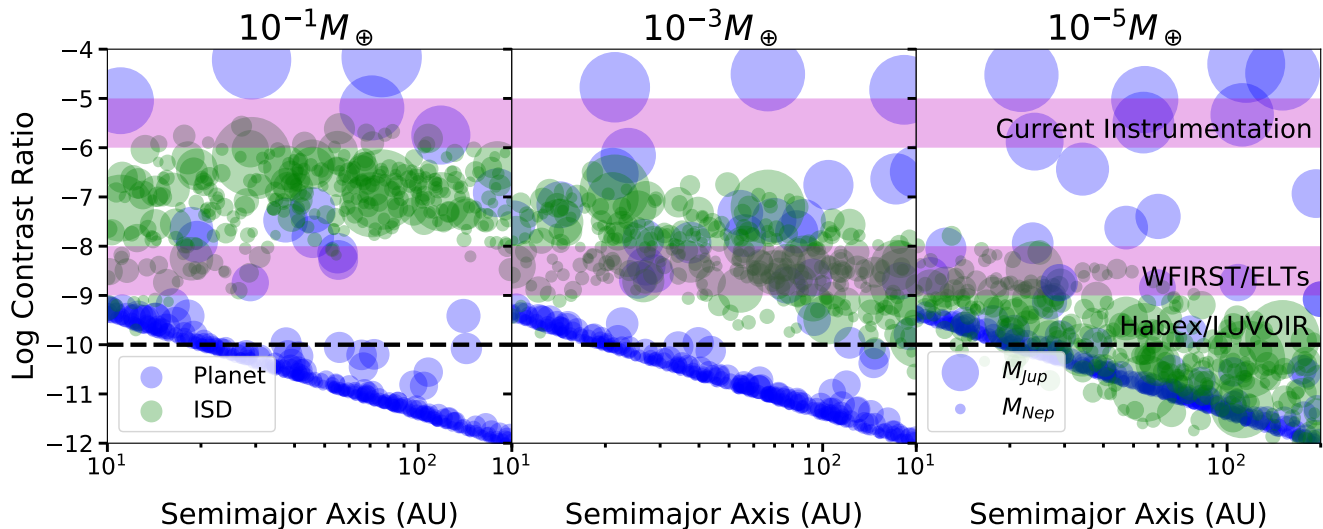
Figure 6. Contrast ratios for 300 ISD realizations around M1 stars in the β Pic moving group. This is much larger than the number of such targets available, and just meant to statistically sample the distribution and show the probability of detection given various thresholds (magenta bands and dashed black line). Blue and green circles are the planet's and ISD's signal, respectively. Circle size is proportional to planetary mass (see legend). Each panel corresponds to a different initial mass in irregular satellites.

group, with distances drawn from a gaussian distribution centered at 35 pc and standard deviation of 10 pc, to approximately match the observed distances from $20 - 50$ pc (Zuckerman et al. 2001). All ISDs are assigned the moving group's estimated age of 25 Myr (Zuckerman et al. 2001; Malo et al. 2014). We draw planet and swarm parameters as described in Sec. 4.2. Planet thermal emission and radii (for calculating the scattered light) are derived by interpolating the same models from Baraffe et al. (2008) as a function of mass, with a heavy element mass fraction $Z = 0.02$ (which should yield optimistically large planets and associated scattered light signals). For the planetary scattered light we assume a phase function of 0.32, and a geometric albedo of 0.4.

The largest uncertainty in our model is the total initial swarm mass. We therefore separate out this dependency and make projections for three different initial mass scales in irregular satellites, roughly centered on the initial masses estimated for our solar system in Sec. 4.1 of $10^{-3} M_\oplus$. We sample 300 planets with ISDs in each panel of Fig. 6. This is much larger than the number of M dwarfs kwown in the beta pic moving group, and simply chosen to statistically sample the distribution of likely contrast ratios. Finally, we consider observing in the H-band at $\approx 1.65 \mu m$, with the wide field of view of the IRDIS instrument on SPHERE, which is able to capture the full relevant range of semimajor axes from 10-200 AU at these target distances (concentration in a blue line).

We see from Fig. 6 that, as expected from detections to date, several of the largest planets (large blue circles, see legend) are detectable through their thermal emission. However, the much more common low-mass Neptunes have negligible thermal emission, and their scattered light signal in the 10-200 AU range is very weak, falling off quadratically with distance from their host star.

By contrast, ISDs (green circles) around planets of all sizes have comparable contrast ratios in each panel, as can be understood from the weak planet-mass scaling in Eq. 12. And indeed, planets around these optimized targets should be readily detectable by WFIRST and next-generation ELT instruments (objects above the corresponding magenta band) over most of the expected range in parameters. Traversing panels from left to right, one can also see

the peak at a_{opt} shifting toward smaller semimajor axes. At $10^{-1} M_\oplus$ the peak is at $\sim 50 AU$ (Eq. 10), and by $10^{-5} M_\oplus$ has dropped to $\sim 5 AU$, so that all ISDs in the right panel are to the right of the contrast peak in the age-limited regime, where contrasts fall off quadratically like for the planets. In all cases, the ISD scattered light signal is significantly larger than that of the planet.

4.6 Direct Imaging of Exoplanet Atmospheres

One might worry that bright ISDs might interfere with efforts to characterize the atmospheres of close-in planets with next-generation instrumentation that would target known planets discovered through radial velocities. However, those planets are typically Gyrs old and, crucially, much further in. For example, the set of radial velocity planets considered by Traub et al. (2014) for WFIRST have semimajor axes of $\approx 1 AU$. The combination of ~ 100 times older planets $\sim 10\times$ farther in would result in contrast ratios a factor of $\sim 10^4$ times smaller than at the left edge of each of the panels in Fig. 6 (specifically targeting M1 stars). Thus, even with optimistic initial swarm masses, contrast ratios from ISDs would be comfortably below 10^{-10}. In the regime close to the host star where giant planets will be detectable through direct imaging in scattered light, ISDs would have ground down enough not to interfere with observations.

4.7 Competition from circumstellar debris disks

Pushing to progressively smaller contrast ratios, one increasingly worries about interference from circumstellar debris, analogues to debris in the Kuiper belt of our solar system. If one boosts estimated dust levels in the outer solar system by even a factor of 100, this debris would only yield contrast ratios at the level of 10^{-9} at tens of AU (Traub et al. 2014). However, the Herschel DEBRIS survey estimated that $28 \pm 3\%$ of FGK stars had circumstellar disks with contrast ratios greater than 5×10^{-6} at similar distances, with the fraction decreasing toward later stellar types (Sibthorpe et al. 2018).

At lower contrast ratios, and pushing toward the lower stellar masses considered above, things become much more uncertain. However, one would expect that the confounding effects of circumstellar debris would at least be weaker at the tens of AUs where ISDs are brightest than at the AU scales where planets would be imaged directly in reflected light.

5 CONCLUSION

Direct imaging surveys have revealed that young super-Jupiters detectable through their thermal emission are rare (Nielsen et al. 2019). Next generation instruments will therefore target weaker scattered light signals from known, close in planets that intercept a larger fraction of starlight. However, by increasing planets' scattering area by orders of magnitude, irregular satellite disks (ISDs) can even render far out Neptunes detectable.

We investigated ISD properties and detectability following models for their collisional evolution from Kennedy & Wyatt (2011). Such structures would typically be optically thin, polarized, and unresolved. Detecting polarized point sources can rule out background sources or other false positives to high confidence in a single epoch. One could also more aggressively suppress the unpolarized speckle noise to improve sensitivity. We provide analytic expressions for their expected contrast ratios as a function of stellar, planetary and swarm parameters (Sec. 3), as well as open-source code for ease of calculation and reproduction of the figures in this paper https://github.com/LoicNassif/CE-Irregular-Satellites. This makes it straightforward to make predictions for different instruments and observation strategies.

Planets are brightest in scattered light closer to their host star where they intercept more starlight. At these distances, inside ~ 1 AU, ISDs will have typically ground away (Sec. 4.6), and will therefore not interfere with atmospheric characterization efforts. By contrast, scattered light signals from ISDs are brighter at larger semimajor axes, typically peaking in the $\sim 10 - 100$ AU range where the exoplanet sample is sparsest. Indeed, over a wide range of parameters, we expect that the majority of planetary signals with contrast ratios $\sim 10^{-9} - 10^{-6}$ should be due to ISDs at these long periods (Sec. 4.5). Furthermore, the weak scalings with planetary mass and system age render a wide diversity of planets detectable (Sec. 3.1).

Below contrast ratios of $\sim 10^{-6}$, once integration times begin to be measured in days, efficient observation strategies shift from discovery of new planets to characterization of planets discovered by alternate methods. In this regime, wide fields of view like that of the IRDIS instrument on SPHERE would be a considerable asset for serendipitous detections. This would allow programs to characterize the atmospheres of known planets at ~ 1 AU to simultaneously detect ice giant ISDs out to ~ 100 AU. This provides a complementary and compelling science case, inaccessible to other detection methods, which would elucidate the early lives of planetary systems (Sec. 1.2).

6 ACKNOWLEDGEMENTS

REFERENCES

ALMA Partnership Brogan C. L., et al. 2015, arXiv preprint arXiv:1503.02649

Andrews S. M., et al., 2018, The Astrophysical Journal Letters, 869, L41

Baraffe I., Chabrier G., Barman T., 2008, Astronomy & Astrophysics, 482, 315

Benz W., Asphaug E., 1999, Icarus, 142, 5

Béthune W., Lesur G., Ferreira J., 2016, Astronomy & Astrophysics, 589, A87

Bottke W. F., Nesvorný D., Vokrouhlický D., Morbidelli A., 2010, AJ, 139, 994

Bowler B. P., Nielsen E. L., 2018, Handbook of Exoplanets, pp 1–17

Bowler B. P., Liu M. C., Dupuy T. J., Cushing M. C., 2010, The Astrophysical Journal, 723, 850

Brouwers M., Ormel C., 2019, arXiv preprint arXiv:1908.02742

Burns J. A., Lamy P. L., Soter S., 1979, Icarus, 40, 1

Chatterjee S., Ford E. B., Matsumura S., Rasio F. A., 2008, ApJ, 686, 580

Chiang E., Laughlin G., 2013, Monthly Notices of the Royal Astronomical Society, p. stt424

Chilcote J., et al., 2014, The Astrophysical Journal Letters, 798, L3

Clanton C., Gaudi B. S., 2016, The Astrophysical Journal, 819, 125

Collier Cameron A., Horne K., Penny A., Leigh C., 2002, Monthly Notices of the Royal Astronomical Society, 330, 187

Ćuk M., Burns J. A., 2004, Icarus, 167, 369

Ćuk M., Gladman B. J., 2006, Icarus, 183, 362

Cumming A., Butler R. P., Marcy G. W., Vogt S. S., Wright J. T., Fischer D. A., 2008, Publications of the Astronomical Society of the Pacific, 120, 531

De La Reza R., Jilinski E., Ortega V., 2006, The Astronomical Journal, 131, 2609

Deienno R., Morbidelli A., Gomes R. S., Nesvornỳ D., 2017, The Astronomical Journal, 153, 153

Dipierro G., Price D., Laibe G., Hirsh K., Cerioli A., Lodato G., 2015, Monthly Notices of the Royal Astronomical Society: Letters, 453, L73

Donaldson J. K., Weinberger A. J., Gagné J., Faherty J. K., Boss A. P., Keiser S. A., 2016, The Astrophysical Journal, 833, 95

Droettboom M., et al., 2016, matplotlib: matplotlib v1.5.1, doi:10.5281/zenodo.44579, http://dx.doi.org/10.5281/zenodo.44579

Ducourant C., Teixeira R., Galli P. A. B., Le Campion J., Krone-Martins A., Zuckerman B., Chauvin G., Song I., 2014, Astronomy & Astrophysics, 563, A121

Flock M., Ruge J., Dzyurkevich N., Henning T., Klahr H., Wolf S., 2015, Astronomy & Astrophysics, 574, A68

Gagné J., et al., 2017, The Astrophysical Journal Supplement Series, 228, 18

Goldreich P., Lithwick Y., Sari R., 2004, The Astrophysical Journal, 614, 497

Gould A., et al., 2010, The Astrophysical Journal, 720, 1073

Hamilton D. P., Skrutskie M. F., Verbiscer A. J., Masci F. J., 2015, Nature, 522, 185

Heng K., Tremaine S., 2010, Monthly Notices of the Royal Astronomical Society, 401, 867

Hunter J. D., 2007, Computing In Science & Engineering, 9, 90

Janson M., Bergfors C., Goto M., Brandner W., Lafrenière D., 2010, The Astrophysical Journal Letters, 710, L35

Johansen A., Lambrechts M., 2017, Annual Review of Earth and Planetary Sciences, 45, 359

Jurić M., Tremaine S., 2008, ApJ, 686, 603

Kalas P., et al., 2008, Science, 322, 1345

Kalas P., Graham J. R., Fitzgerald M. P., Clampin M., 2013, preprint, (arXiv:1305.2222)

Kennedy G. M., Wyatt M. C., 2011, MNRAS, 412, 2137

Kluyver T., et al., 2016, Positioning and Power in Academic Publishing: Players, Agents and Agendas, p. 87

Kruegel E., 2003, The physics of interstellar dust

Lagrange A.-M., et al., 2010, ScienMiddle East Technical Universityce, 329, 57

Lambrechts M., Johansen A., 2012, Astronomy & Astrophysics, 544, A32

Lee E. J., Chiang E., 2015, The Astrophysical Journal, 811, 41

Lee E. J., Chiang E., Ormel C. W., 2014, Make super-Earths, not Jupiters: Accreting nebular gas onto solid cores at 0.1 AU and beyond

Leinhardt Z. M., Stewart S. T., 2009, Icarus, 199, 542

Lorén-Aguilar P., Bate M. R., 2015, Monthly Notices of the Royal Astronomical Society: Letters, 453, L78

Malo L., Doyon R., Feiden G. A., Albert L., Lafrenière D., Artigau É., Gagné J., Riedel A., 2014, The Astrophysical Journal, 792, 37

Marois C., Macintosh B., Barman T., Zuckerman B., Song I., Patience J., Lafrenière D., Doyon R., 2008, Science, 322, 1348

Morbidelli A., Nesvorny D., Laurenz V., Marchi S., Rubie D., Elkins-Tanton L., Wieczorek M., Jacobson S., 2018, Icarus, 305, 262

Nesvornỳ D., 2018, Annual Review of Astronomy and Astrophysics, 56, 137

Nesvorný D., Vokrouhlický D., Morbidelli A., 2007, AJ, 133, 1962

Nielsen E. L., et al., 2019, arXiv preprint arXiv:1904.05358

Ochsenbein F., Bauer P., Marcout J., 2000, Astronomy and Astrophysics Supplement Series, 143, 23

Pérez F., Granger B. E., 2007, Computing in Science and Engineering, 9, 21

Pinte C., Dent W. R., Ménard F., Hales A., Hill T., Cortes P., de Gregorio-Monsalvo I., 2015, The Astrophysical Journal, 816, 25

Pinte C., et al., 2018, The Astrophysical Journal Letters, 860, L13

Piso A.-M. A., Youdin A. N., 2014, The Astrophysical Journal, 786, 21

Pollack J. B., Burns J. A., Tauber M. E., 1979, Icarus, 37, 587

Pollack J. B., Hubickyj O., Bodenheimer P., Lissauer J. J., Podolak M., Greenzweig Y., 1996, Icarus, 124, 62

Popper D. M., 1980, ARA&A, 18, 115

Rosenthal M., Murray-Clay R., 2018, The Astrophysical Journal, 864, 66

Ruffio J.-B., et al., 2017, The Astrophysical Journal, 842, 14

Schlichting H. E., 2014, The Astrophysical Journal Letters, 795, L15

Sibthorpe B., Kennedy G. M., Wyatt M. C., Lestrade J. F., Greaves J. S., Matthews B. C., Duchêne G., 2018, MNRAS, 475, 3046

Szulágyi J., Plas G. v. d., Meyer M. R., Pohl A., Quanz S. P., Mayer L., Daemgen S., Tamburello V., 2018, MNRAS, 473, 3573

Szulágyi J., Dullemond C., Pohl A., Quanz S., 2019, Monthly Notices of the Royal Astronomical Society

Takahashi S. Z., Inutsuka S.-i., 2014, The Astrophysical Journal, 794, 55

Tamayo D., Burns J. A., Hamilton D. P., Hedman M. M., 2011, Icarus, 215, 260

Tamayo D., Hedman M. M., Burns J. A., 2014, Icarus, 233, 1

Tamayo D., Triaud A. H., Menou K., Rein H., 2015, The Astrophysical Journal, 805, 100

Tamayo D., Markham S. R., Hedman M. M., Burns J. A., Hamilton D. P., 2016, Icarus, 275, 117

Teague R., Bae J., Bergin E. A., Birnstiel T., Foreman-Mackey D., 2018, The Astrophysical Journal Letters, 860, L12

Traub W. A., et al., 2014, in Space Telescopes and Instrumentation 2014: Optical, Infrared, and Millimeter Wave. p. 91430N

Tsiganis K., Gomes R., Morbidelli A., Levison H. F., 2005, Nature, 435, 459

Verbiscer A. J., Skrutskie M. F., Hamilton D. P., 2009, Nature, 461, 1098

Wyatt M. C., Smith R., Greaves J., Beichman C., Bryden G., Lisse C., 2007, the Astrophysical Journal, 658, 569

Wyatt M. C., Booth M., Payne M. J., Churcher L. J., 2010, MNRAS, 402, 657

Zhang K., Blake G. A., Bergin E. A., 2015, The Astrophysical Journal Letters, 806, L7

Zhang S., et al., 2018, ApJ, 869, L47

Zuckerman B., Song I., Bessell M., Webb R., 2001, The Astrophysical Journal Letters, 562, L87